

# Nanoscale Investigation and Control of Photothermal Action of Gold Nanostructure-coated Surfaces

**Samir V Jenkins**

University of Arkansas for Medical Sciences <https://orcid.org/0000-0003-1496-2035>

**Seunghyun Jung**

University of Arkansas for Medical Sciences

**Shruti Shah**

University of Arkansas for Medical Sciences

**Paul C Millett**

University of Arkansas Fayetteville

**Ruud P.M. Dings**

University of Arkansas for Medical Sciences

**Michael J. Borrelli**

University of Arkansas for Medical Sciences

**Robert J. Griffin** (✉ [rjgriffin@uams.edu](mailto:rjgriffin@uams.edu))

Departments of Radiation Oncology, University of Arkansas for Medical Sciences, Little Rock AR  
<https://orcid.org/0000-0002-3574-2958>

---

## Research

**Keywords:** Gold nanoparticles, Thermal dose, Photothermal, Cell-culture surfaces

**Posted Date:** September 23rd, 2020

**DOI:** <https://doi.org/10.21203/rs.3.rs-76256/v1>

**License:** © ⓘ This work is licensed under a Creative Commons Attribution 4.0 International License.

[Read Full License](#)

---

**Version of Record:** A version of this preprint was published at Journal of Materials Science on March 8th, 2021. See the published version at <https://doi.org/10.1007/s10853-021-05947-6>.

1 **Nanoscale Investigation and Control of Photothermal Action of Gold Nanostructure-coated**  
2 **Surfaces**

3 Samir V. Jenkins,<sup>1</sup> Seunghyun Jung,<sup>2</sup> Shruti Shah,<sup>1</sup> Paul C. Millett,<sup>3</sup> Ruud P.M. Dings,<sup>1</sup> Michael  
4 J. Borrelli,<sup>4</sup> Robert J. Griffin<sup>1\*</sup>

5  
6 Departments of <sup>1</sup>Radiation Oncology, <sup>2</sup>Physiology, and <sup>4</sup>Radiology; University of Arkansas for  
7 Medical Sciences, Little Rock AR

8 <sup>3</sup>Department of Mechanical Engineering, University of Arkansas, Fayetteville, AR

9 \*Corresponding Author: Robert J. Griffin ([rjgriffin@uams.edu](mailto:rjgriffin@uams.edu), F: 5016867285)

10

11 Keywords: Gold nanoparticles, Thermal dose, Photothermal, Cell-culture surfaces,

12 **Abstract**

13 *Background:* The combination of biological variation and nanomaterial heterogeneity makes  
14 elucidating the mechanisms of interactions between cells and nanoparticles extremely  
15 complicated. Accurate nanoparticle quantification can be extremely challenging, and cellular  
16 response can change based on the location of the nanoparticle and the cell type under investigation.

17 These complications are only augmented by the additional of external stimuli. These limitations  
18 have yielded a wide range of studies that show effects, but often provide little mechanistic insight.

19 *Results:* Gold nanomaterials were stably immobilized onto glass coverslips treated with  
20 mercaptosilane to control both the average number of nanoparticles that interact with cells and  
21 their spatial orientation relative to the cell membrane. Surfaces were characterized optically and  
22 by electron microscopy to confirm their surface density and uniformity. The thermal response of  
23 Au nanocage-coated surfaces to near infrared laser irradiation was measured in cell culture

24 medium and modelled computationally. The modelling showed a vastly higher thermal dose than  
25 would be predicted by bulk temperature measurements. Adherent or non-adherent cell lines were  
26 cultured directly on the nanocage-coated surface or in the medium, respectively, in culture wells  
27 and laser irradiation was applied. Survival of cells growing in suspension correlated with the bulk  
28 temperature increase in the culture medium, as measured by viability assay. Conversely, adherent  
29 cells exhibited a much greater susceptibility than expected from the bulk temperature  
30 measurement, which is ostensibly related to the close interaction with the nanoparticles on their  
31 growth substrate and induction of substantially greater thermal dose upon laser exposure.

32 *Conclusions:* This platform is designed to be a new tool to determine how many particles need to  
33 be in contact with a cell to induce desired physical or biological effects. Here we demonstrate the  
34 delivery of precise thermal doses following laser irradiation. The anticipated biological effects  
35 based on bulk measurements vastly underestimated the effects that were observed, which is  
36 ascribed to the proximity of the nanoparticle to the cell and the extraordinary high surface  
37 temperature of the particle. This platform could be expanded to a variety of nanoparticles, external  
38 stimuli, and cell types to enable more deliberate and optimized application of nanomedicine.

39

## 40 **Background**

41           Local thermal therapy is an attractive, emerging treatment modality for biomedical  
42 conditions requiring sterilization or ablation of pathological tissue features. This localized  
43 treatment can be precisely delivered by combining absorbing nanoparticles with optical or  
44 magnetic<sup>1</sup> fields. Plasmonic nanoparticles, particularly gold-based particles (AuNPs), are under  
45 intense investigation as thermal transducers due to their strong electromagnetic absorption,<sup>2</sup>  
46 biocompatibility,<sup>3</sup> surface functionalizability,<sup>4</sup> and potential for on-demand drug delivery.<sup>5</sup>  
47 However, there is a paucity of methods to determine precise effects due to heterogeneous  
48 biological responses in culture or tissues and from nanoparticle composition variability. Setting  
49 aside the myriad complexities involved in *in vivo* systems, there is a vast degree of heterogeneity  
50 even at a cellular level. The cell association values (*i.e.* the number of particles per cell) are  
51 typically calculated after incubation with the particles. This alone has been demonstrated to show  
52 a wide Gaussian curve of particle number per cell using means such as single particle ICP-MS,  
53 flow cytometry, and optical and electron microscopy.<sup>6-8</sup> This limitation is further complicated by  
54 the cellular localization of particles, which may be membrane bound,<sup>9</sup> cytosolic,<sup>10</sup> endosomally  
55 encapsulated,<sup>11</sup> nuclear<sup>12</sup> or some combination thereof. Additionally, these measurements require  
56 multiple preparatory steps to ascertain final values, which include collection of cells, washing, and  
57 work-up. As a result, the quantification of the particle association with cells is indirect and  
58 experimentally averaged. Technical limitations severely impede the ability to directly measure  
59 these materials microscopically *in situ* in a large, statistically-relevant population.<sup>13</sup> In addition to  
60 these preparatory steps, the variable distribution of particles per cell further modulates the dose  
61 received by individual cells.<sup>14</sup> Even the determination of particle concentration prior to incubation  
62 is a challenging task that can affect outcomes.<sup>15</sup> Ultimately the dose is treated as a bulk average.

63 This issue is akin to the distinction between bulk optical properties and single-molecule studies.<sup>16</sup>  
64 As a result of these factors, correlating the *in vitro* dose at the level of the particle vs. the bulk  
65 culture becomes a largely arbitrary and unreliable endeavor.

66 Applying light to induce thermal dose from particles is one of the more thoroughly studied  
67 means of achieving local nanomaterial therapeutic effects.<sup>17</sup> To date, characterizing the response  
68 to laser-induced nanoparticle heating generally relies on indirect evidence *via* bulk solution  
69 temperature measurements. An ongoing challenge for the validation of the mechanism of action  
70 of these materials upon non-invasive stimulation by light is the determination of true “thermal  
71 dose.” Thermal dose can be practically defined as the amount of heat received by an individual  
72 cell or particular volume in a given time.<sup>18,19</sup> Traditional non-ablative hyperthermic treatment uses  
73 multi-hour heating with a temperature change of only a few degrees above body temperature (<43  
74 °C).<sup>20</sup> Conversely, many nanoparticle heating studies utilize extremely short heating durations  
75 caused by rapid absorption of pulses of light with analogous bulk temperature changes.<sup>21</sup> While  
76 the temperature changes and therapeutic outcomes are often similar, the difference in the  
77 time\*temperature product – which estimates thermal dose<sup>22</sup> – strongly suggests dramatic  
78 divergences among local heating effects. The most common thermal dose metric is the cumulative  
79 equivalent minutes at 43 °C (CEM43).<sup>23,24</sup> Further, numerous studies have shown that cell-specific  
80 targeting leads to greatly enhanced ‘thermal’ effects relative to similar temperature profiles with  
81 untargeted particles.<sup>25</sup> A variety of pre-clinical studies have observed distinctly different effects  
82 between untargeted materials and targeted materials using ligands for  $\alpha 1\beta v$ ,<sup>26</sup> epithelial growth  
83 factor receptor,<sup>27</sup> or galectin-1,<sup>28, 29</sup> and this has been further demonstrated *in vitro* in bacterial  
84 biofilm models.<sup>30</sup> It is under debate whether this enhancement is the result of increased  
85 accumulation, minimal spatial separation of particles and cells, or a combination thereof. As such,

86 the resultant cellular response to photothermal stress would not be anticipated based purely on  
87 bulk temperature effects.<sup>31</sup> The extreme variance on a per cell basis regarding particle uptake  
88 combined with the relatively extreme heating at the nanoparticle surface (a highly irregular  
89 time/temperature history)<sup>32</sup> limits the mechanistic utility of many *in vitro* studies, and both  
90 measuring and calculating these temperatures are nontrivial tasks.<sup>33</sup> As a result, the precise  
91 response to these extreme heating conditions is not well understood experimentally.

92         Toward the end of thoroughly understanding and controlling nanoparticle induced heat  
93 effects, this report demonstrates a novel nanomaterial validation platform that employs  
94 nanomaterial coated surfaces to induce, characterize, and apply precise thermal doses to cells  
95 cultured upon them. This method's utility was demonstrated with a variety of nanoparticle  
96 morphologies including Au nanocages (AuNCs), nanorods (AuNRs), and nanospheres (AuNSs).  
97 Indeed, these particles function like very small heaters upon laser irradiation and induce biological  
98 effects on nearby, attached cells to a much different extent than bulk temperature would suggest,  
99 which was validated with theoretical modelling. This change in heating was demonstrated through  
100 photothermal killing of adherent cells, while under identical conditions suspension cells were  
101 minimally affected. The different biological outcomes despite similar temperature measurements  
102 are discussed, providing a context for similar studies that rely on strong local effects from  
103 nanoparticles themselves, such as drug delivery or ionizing radiation enhancement.

## 104 **Materials and Methods**

### 105 Reagents

106 Silver trifluoroacetate (AgTFA), sodium hydrogen sulfide (NaSH), hydrochloric acid (HCl,  
107 99.999%), tetrachloroauric acid trihydrate (HAuCl<sub>4</sub>·3H<sub>2</sub>O), sodium chloride (NaCl), and were  
108 purchased from Alfa Aesar. Poly(vinylpyrrolidone) (PVP, M.W.=55,000), sodium carbonate

109 (Na<sub>2</sub>CO<sub>3</sub>), sodium bicarbonate (NaHCO<sub>3</sub>), methanol (MeOH) concentrated sulfuric acid (H<sub>2</sub>SO<sub>4</sub>),  
110 nitric acid (HNO<sub>3</sub>), hydrochloric acid (HCl), and 30% hydrogen peroxide (H<sub>2</sub>O<sub>2</sub>), 3-  
111 aminopropyltrimethoxysilane (APTMS), and 3-mercaptopropyltrimethoxysilane (MPTMS)  
112 were purchased from Sigma Aldrich. Ethylene glycol (EG) was purchased from J.T. Baker.  
113 Acetone was purchased from EMD. Au nanospheres, nanorods, and nanocubes were purchased  
114 from Nanocomposix (San Diego). All experiments were performed using 18 MΩ H<sub>2</sub>O unless  
115 specified otherwise. All chemicals were used as received.

#### 116 *AuNC Preparation*

117 AuNCs were synthesized using the galvanic replacement reaction between the Ag nanocubes and  
118 tetrachloroauric acid in aqueous solution modified from previous publications.<sup>34</sup> The Ag  
119 nanocubes were prepared by the modified polyol process. Briefly, ethylene glycol (EG; 50 ml)  
120 was added into a 250 ml round bottom flask and heated to 150 °C in air, without a condenser. To  
121 the reaction, 3 mM NaSH in EG (0.6 ml), 3 mM HCl in EG (5 ml), 180 mM polyvinylpyrrolidone  
122 (PVP; 12.5 ml) and 325 mM silver trifluoroacetate (4 ml) were added into the preheated EG in the  
123 above sequence. The color of the reaction changed from yellow to dark red, reddish grey and  
124 brown, indicating the formation of the Ag nanocubes with desired edge length (35–40 nm) and  
125 LSPR ~430 nm. The Ag nanocubes were collected by centrifugation, purified with acetone and  
126 resuspended in 10 ml of water. For the galvanic replacement, the Ag nanocubes (2 ml) were added  
127 to 20 ml of boiling H<sub>2</sub>O. After the solution re-established thermal equilibrium (~2 min), 1 mM  
128 HAuCl<sub>4</sub> aqueous solution was titrated at a rate of 45 ml/h until the absorbance maximum reached  
129 800 nm. The solution was kept on heat for another 5 min, and then allowed to cool to room  
130 temperature. This process was repeated for several batches, which were ultimately combined. The

131 resultant AuNCs were washed with saturated NaCl to solubilize AgCl and subsequently three times  
132 with water.

### 133 *Surface Preparation*

134 Surface preparation for AuNC coated surfaces was achieved as follows. Necessary adjustments  
135 for other AuNP morphologies are found in **Table 1**. Glass cover slips (circular, 12.5 mm diameter)  
136 were initially pretreated with *aqua regia* (3:1 HCl:HNO<sub>3</sub>) then treated for 60 min at 60-65 °C with  
137 piranha solution (3:1 H<sub>2</sub>SO<sub>4</sub>:H<sub>2</sub>O<sub>2</sub>) in glass petri dishes. (NOTE: Piranha solution is extremely  
138 corrosive and must be handled cautiously with adequate PPE including goggles, lab coat, and  
139 gloves). The reaction was quenched with 2 washes with DI H<sub>2</sub>O, followed by 2 rinses with 100%  
140 MeOH. Surfaces were then submerged in MeOH with 10% (trimethoxy)-mercaptopropyl silane  
141 for 60 - 72 h at 37 °C. Surfaces were then washed thrice with 100% MeOH and set in individual  
142 wells of a 24-well plate that contains 1 mL of 100% MeOH. The 24 well plate containing the  
143 silanized coverslips was sonicated in a bath sonicator (Fisher) for 10 min. Surfaces were washed  
144 twice with 100% MeOH. The glass coverslips were cured at 100 °C for 5 min. Au nanoparticles  
145 were added in varying aqueous buffers and concentrations in 1 mL and the reaction was allowed  
146 to proceed overnight at 37 °C. The best results were obtained with AuNCs (6.4, 12.8, or 25.6 fmol  
147 in 1 mL) added to sodium carbonate-bicarbonate buffer (pH = 9.1, 5 mM) Surfaces were then  
148 washed with DI H<sub>2</sub>O and allowed to dry in the plate. Sterilization was achieved by removing the  
149 lid from the plate in a biosafety cabinet and running the UV cycle.

### 150 *Surface Characterization*

151 The specimens deposited on glass slides were mounted onto 12.2 mm dia. x10 mm high aluminum  
152 disks (Ted Pella, Inc. Redding, CA) by double sided carbon tapes, and their surfaces were covered  
153 by ~3nm thick carbon films as conductive coatings. The carbon films were deposited by Gatan

154 681 Ion Beam Coater (Gatan, Inc. Pleasanton, CA). The specimens were then mounted on a  
155 stainless steel specimen holder, and their edges were grounded to the holder by conductive copper  
156 tapes. before being inserted into a JEOL JSM-7000F (JEOL USA, Peabody, MA) field emission  
157 scanning electron microscope (SEM). A series of secondary electron images with varying  
158 magnifications on each specimen were obtained at specimen bias ranging from 5kV to 15kV.

### 159 *Cell Culture*

160 4T1 (murine breast carcinoma) and EL4 (murine leukemia) cells were purchased from ATCC (Cat.  
161 No. CRL-2539 and TIB-39). Cells were cultured in DMEM containing 10% FBS and 1% P/S and  
162 passaged biweekly. Cells were incubated at 37 °C, with 90% humidity and 5% CO<sub>2</sub>.

### 163 *Photothermal Treatment*

164 Surfaces in wells were covered with 1 mL of cell culture media prior to laser application. The laser  
165 spot size was adjusted to 12.5 mm diameter, and the power was adjusted to control fluence.  
166 Temperature measurements were taken with a thermal couple applied directly to the coverslip at 2  
167 min intervals, during which laser illumination was briefly halted (<5 sec).

168 4T1 cells were seeded at 5000 cells per well in a 200 µL drop on the sterilized particle-coated  
169 surface. After being allowed to adhere for 3 h, an additional 800 µL of media was added to bring  
170 the final volume to 1 mL. EL4 cells were directly applied as 5000 cells in 1 mL. The plates were  
171 allowed to equilibrate to room temperature for 30 min prior to laser application. Laser irradiation  
172 was applied using a Diomed 25 at 808 nm with a fluence of 0.75 W/cm<sup>2</sup> for 10 min. Cells were  
173 then returned to incubation at 37 °C and allowed to grow for 3 days prior to measurement of cell  
174 viability *via* CCK-8 assay (Dojindo). All cell viability measurements were normalized to cells  
175 grown on standard tissue culture wells without glass surfaces or laser treatment and run in  
176 triplicate.

177 For bulk heating experiments, cells were seeded at 1000 cells/well in standard tissue culture 96-  
 178 well plates. After 3 hours, plates were sealed with parafilm, enclosed in plastic bags and submerged  
 179 in a circulating water bath (Thermo DC10) at 37-50 °C for 10 min (or 1 h at 42.5 °C). Plates were  
 180 unsealed and returned to the incubator following treatment and viability was measured after 3 days  
 181 using CCK-8.

182 *Theoretical Modelling*

183 The temperature distribution resulting from the photothermal excitation of a nanoparticle (or a  
 184 system of nanoparticles) can be modeled with the standard heat transfer equation:

$$185 \quad c\rho \frac{\partial T(\mathbf{r},t)}{\partial t} = k \frac{\partial^2 T(\mathbf{r},t)}{\partial r^2} + Q(\mathbf{r}, t) \quad (1)$$

186 where  $T(\mathbf{r}, t)$  is the coordinate- and time-dependent temperature,  $Q(\mathbf{r}, t)$  is the volumetric heat  
 187 source term (units of W/m<sup>3</sup>), and  $c$ ,  $\rho$ , and  $k$  are the heat capacity, density, and thermal  
 188 conductivity of the medium, respectively. Following Govorov et al.<sup>35</sup> the steady-state temperature  
 189 profile extending radially from a single (spherical) nanoparticle heat source is:

$$190 \quad \Delta T_o(\mathbf{r}) = \frac{V_{NP}Q}{4\pi kr} \quad (r > R_{NP}) \quad (2)$$

191 where  $R_{NP}$  and  $V_{NP}$  are the radius and volume of the nanoparticle. Govorov et al. further considered  
 192 a superstructure of  $N_{NP}$  nanoparticle heat sources arranged in  $m$ -dimensional space, for which the  
 193 temperature distribution was derived as (for  $m \geq 2$ ):

$$194 \quad \Delta T(\mathbf{r}) \approx \Delta T_o(\mathbf{r}) \frac{R_{NP}}{p} N_{NP}^{(m-1)/m} \quad (3)$$

195 where  $p$  is the average spacing between nanoparticles.<sup>35</sup> For this work, we assume  $m = 2$  and the  
 196 thermal conductivity of water = 0.6 W/m/K = 6e-7 W/μm/K.

197 Calculation of CEM43 values was performed using

$$198 \quad CEM43 = \sum_{i=1}^n t_i \times R^{(43-T_i)} \quad (4)$$

209 where CEM43 is the cumulative number of equivalent minutes at 43 °C,  $t$  is time,  $T_i$  is temperature  
200 at the  $i$ -th time interval, and  $R$  is related to the temperature dependence of cell death such that  
201 when  $T_i < 43$  °C,  $R = 1/4$  and when  $T_i > 43$  °C  $R = 1/2$ .<sup>23</sup> In Eq. (4),  $T_i$  values were determined  
202 based on the average temperature from 0.05 to 5  $\mu\text{m}$  as determined by Eq. (3).

## 203 **Results**

204 AuNCs were synthesized and found to be >99% cubic nanostructures with an edge length  
205 of approximately 50 nm. AuNCs were coated onto glass coverslips according to **Scheme 1**. It was  
206 found that a crucial step in the synthetic process was the rapid (within several minutes) use of  
207 silanized coverslips following either methanol washing or storage in methanol. These materials  
208 were found to be stable during washing with H<sub>2</sub>O and resistant to solvents such as ethanol (70%)  
209 and dimethyl sulfoxide (DMSO). They were visually uniform (**Fig. 1A**) and showed an even  
210 distribution under optical microscopy (**Fig. 1B-E**), despite the presence of some salt crystals, and  
211 they demonstrated a coverage dependent extinction (**Fig. 1F**).

212 AuNCs were used for further studies as they were found to be the most synthetically  
213 cooperative materials at the outset of experiments. Additionally, AuNCs have been found to have  
214 larger extinction coefficients than AuNRs and AuNSs, particularly at the 808 nm laser wavelength  
215 used. Scanning electron microscopy images showed a highly uniform surface coverage and  
216 varying the initial AuNC quantity from 6.4 to 12.8 and 25.6 fmol AuNC yielded coverage of  $20 \pm$   
217  $2$ ,  $32 \pm 2$ , and  $54 \pm 2$  AuNC/ $\mu\text{m}^2$ , respectively (**Fig. 2**). Based on the area of the coverslip (122.7  
218  $\text{mm}^2$ ) the deposition efficiency was 64%, 51%, and 43% respectively. This number does not  
219 include regions of spontaneous flocculation on the surface, which would significantly increase the  
220 calculated deposition efficiency.

221 The kinetics of the deposition showed two phases. A rapid deposition was observed over  
222 the course of the first 8 hours, which was followed by a much slower deposition phase over the  
223 next 5 days. The process could be monitored spectroscopically (**Fig. 3A**), and the increase in  
224 particle coverage density was confirmed using SEM (**Fig. 3B-C**). When taken as a first order  
225 process, the rate constant is  $\sim 0.17 \text{ h}^{-1}$ .

226 Ultimately AuNCs proved the most compliant material, as AuNSs showed significant  
227 responses to salinity, which is attributed to the electrostatic stabilization of the citrate capping-  
228 ligand, and AuNRs showed a tendency to agglomerate and not adhere to the surface, which is  
229 attributed to the enduring and contrary nature of the cetyl trimethyl ammonium bromide (CTAB)  
230 coating. Particle coated surfaces were successfully generated with controllable surface coverage  
231 using moderate adjustments to **Scheme 1**. Adjustments of individual parameters were necessary  
232 depending on particle type (**Table 1**). The most significant changes were made to the salinity and  
233 pH of the reaction solution. AuNSs, AuNRs, and AuNCs were successfully and uniformly adhered  
234 to surfaces (**Fig. 4**).

235 The AuNC coated surfaces were thermally treated with a continuous wave (CW) 808 nm  
236 laser ( $0.25\text{-}1.25 \text{ W/cm}^2$ ), and a thermal couple was used to measure the temperature at the glass  
237 surface in wells containing 1 mL cell culture media, which was used as the bulk temperature of  
238 the media. The temperature change was shown to be dependent on both the laser fluence and the  
239 coverage density (**Fig. 5 A, B**). SEM imaging following laser treatment revealed some  
240 morphological changes, but the gross nanocage structure remained intact (**Fig. 5 C, D**). It is unclear  
241 whether these changes are the result of nanomaterial restructuring, or carbonization of the coating  
242 materials and/or adsorbed proteinaceous material from the medium

243 Theoretical modeling was performed to estimate the temperature profile as a function of  
244 distance from the AuNC coated surfaces into the media. From Eq. (3), it can be seen that the  
245 difference between a planar distribution of multiple nanoparticle heat sources compared to a single  
246 nanoparticle heat source is the factor  $R_{NP}N_{NP}^{(m-1)/m}/p$ . Thus, the heat source  $Q$  can rather be  
247 considered an effective heat source  $\bar{Q} = QR_{NP}N_{NP}^{(m-1)/m}/p$  to be used in Eq. (2). The temperature  
248 change versus  $r$  (**Fig. 6A**) was calculated assuming  $V_{NP} = (0.05 \mu\text{m})^3$  and  $k = 6\text{e-}7 \text{ W}/\mu\text{m}/\text{K}$ . It  
249 was found that an effective heat source of  $\bar{Q} = 1 \text{ W}/\mu\text{m}^3$  resulted in a temperature change of  $8.3^\circ\text{C}$   
250 at a distance of  $2 \mu\text{m}$  from the surface. This temperature change is well within the range of  
251 measured values from the experiments (**Fig. 5 A,B**), thus giving confidence to this chosen value  
252 of  $\bar{Q}$ . With the given values, the maximal temperature change occurring at the surface predicted  
253 by the model is  $330^\circ\text{C}$ . The temperature change curve shown in **Fig. 6A** can be changed to a  
254 temperature curve by adding the far-field temperature of medium, labeled here as  $T_\infty$ . Assuming  
255 the far-field temperature within the wells is gradually increasing with time, a set of temperature  
256 curves can be plotted (**Fig. 6B**). The far-field temperature values were taken from the experimental  
257 measurements for  $54 \text{ AuNC}/\mu\text{m}^2$  and  $0.75 \text{ W}/\text{cm}^2$  irradiation. Temperatures near the coated  
258 surface are affected minimally from the gradual increase in the far-field temperatures. Based on  
259 these measurements and the assumption that the cell has a vertical height of  $5 \mu\text{m}$  CEM43 values  
260 for a given cell in contact with nanocages were calculated (**Fig. 6C**) for each of the measured  
261 temperatures and treated as a Riemann sum (2 min intervals). These values show a thermal dose  
262 to adherent cells that far exceeds the values anticipated based on bulk measurements.

263 Murine breast carcinoma cells (4T1) or murine leukemia cells (EL4) were grown on the  
264 sterilized surfaces. 4T1 cells are adherent cells while EL4 cells are suspension cells, both have  
265 reported doubling times of  $\sim 24 \text{ h}$ . These cells were grown on surfaces with varying coverage

266 density of AuNCs and then treated with  $0.75 \text{ W/cm}^2$  of 808 nm laser, which based on the above  
267 measurements, yielded a maximum temperature in the medium of  $43 \text{ }^\circ\text{C}$  after 10 min (**Fig. 7A**).  
268 Cells were also cultured in standard tissue culture plates and treated in a water bath for 1 h at 42  
269  $^\circ\text{C}$  or 10 min at  $43 \text{ }^\circ\text{C}$ . The EL4 cells were found to respond similarly regardless of whether the  
270 heat source was external water bath-induced bulk heating or laser induced photothermal heating.  
271 The 4T1 cells, however, showed a much greater response to the photothermal heating than to the  
272 bulk heating. Additionally, cells were independently treated with water bath heating for 10 min at  
273 temperatures up to  $50 \text{ }^\circ\text{C}$  (**Fig. 7B**). The 4T1 cellular response to 10 min of photothermal treatment  
274 was similar to 10 min nearly  $50 \text{ }^\circ\text{C}$  in the case of 4T1 cells, which suggests better alignment with  
275 the CEM43 estimate than the measured temperature.

276

## 277 **Discussion**

278 This solution phase deposition provided reliably uniform surfaces. Lithographic techniques  
279 have been demonstrated to produce surfaces with a higher degree of uniformity,<sup>36</sup> but the method  
280 used here enables extremely easy scale up, obviates the need to expensive equipment, and can be  
281 used with any particle morphology. A variety of parameters were tested to identify optimal  
282 conditions for evenly fabricated attachment of different types of nanoparticles onto the silanized  
283 coverslips. Factors such as reaction solution, silane concentration, pH, temperature, and duration  
284 of nanoparticle-functionalized glass reaction were considered. The coverslips were treated with  
285 different concentrations of silanes to maximize the attachment of nanoparticles on the surfaces. As  
286 the concentration of silane was increased from 0 - 10% in methanol, the number of nanoparticles  
287 that attached to the surface increased, and the coverage became saturated at silane concentrations  
288 above 10%. Different reaction buffers such as bicarbonate, carbonate, phosphate, and carbonate-

289 bicarbonate buffer were tested to control the density and aggregation of nanoparticles onto glass  
290 coverslips. The carbonate-bicarbonate buffer showed the best outcome compared to the other  
291 buffers, likely because of its high buffering capacity at pH 9. This buffer proved to be particularly  
292 effective at higher pH, which is likely a result of the increased bonding of Au-thiolate relative to  
293 Au-thiol.<sup>37, 38</sup> However, at extremely high pH (> 12) or salinity (> 20 mM), increases in areas of  
294 nanoparticle aggregation were observed. The pH was determined to be the most critical factor in  
295 efficient, high density coating. The strength of the binding can be partly attributed to the large  
296 number of Au-S bonds between each particle and the surface. There were also two relevant  
297 observations for which we cannot fully account. First, there was significant batch-to-batch  
298 variation observed in the coverage density when we used commercially available particles (rods  
299 and spheres, specifically) regardless of the surface coating (e.g. PEG, citrate, CTAB). Second, in-  
300 house synthesized AuNCs were significantly more agreeable to work with than commercially  
301 available PVP-coated particles, which proved to be inconsistent, prone to aggregation, and to yield  
302 lower coverage density.

303         These results clearly demonstrate that in order to understand different nanomedicine  
304 platforms, the experimental setup must be very tightly controlled to elucidate the true interactions  
305 and dose response requirements. With regard to the photothermal studies presented here, consider  
306 a 0.25 nM solution of (cubic) gold nanocages with a 50 nm edge length. These particles will  
307 ultimately occupy 0.002 % of the solution volume, which means 1 mL of solution will contain  
308 only 20 nL of nanoparticles; yet these particles can achieve extraordinary thermal effects, despite  
309 their volume. By analogy, a kitchen stove can be used to heat an entire dwelling, but the  
310 temperature at the stovetop is much greater than the bulk temperature change of the residence, ergo  
311 the bulk temperature change is not indicative of the locoregional heating. Furthering the analogy,

312 to fry an egg, one must put a skillet directly on the stove, rather than merely adjacent, *i.e.* the  
313 immediate biological effects, such as protein denaturation, are likely the result of the close  
314 proximity to an extremely hot material, rather than bulk thermal changes. The particle system  
315 modeled here represents only a one-dimensional interaction between the surface and the medium.  
316 The particles themselves are spaced out on the surface generating further localized hot spots that  
317 likely result in significant membrane damage peppered across one side of the cell, and the intensity  
318 of these hot spots can be further controlled by varying the laser power density. The sharp increase  
319 in temperature as the particle surface is approached results in the cell observing a significantly  
320 higher local temperature than can be measured in bulk. As a result, calculations of CEM43 yield  
321 orders of magnitude greater thermal dose than based on measured temperatures. These CEM43  
322 values align more closely with the biological results for adherent cells, while the suspension cells  
323 are aligned more closely with bulk temperature measurements. The steep rise in the predicted  
324 temperature at the particle surface provide some explanation for the increased efficacy of targeted  
325 nanomaterials in tumor treatment, as these particles are not merely in the interstitium but closely  
326 bound to the cell, which amplifies the damage.

327         As nanomaterials are continually becoming integrated into biological studies, assessing the  
328 unique and individual properties of each becomes increasingly important. Each cell will likely  
329 interact with a different number of nanoparticles, which could significantly skew results. These  
330 surfaces allow a means to normalize this variance to membrane area, and our methodology is  
331 widely adaptable to a variety of materials. This platform can be used as a screening platform to  
332 more precisely define the thermosensitivity of various cell lines. Our chosen application was  
333 photothermal killing of cancer cells, but there are many other avenues available. There are many  
334 nanoparticle-bound drug complexes in development, and these surfaces could be adapted to

335 provide insight into their efficacy. There is heated debate about the nanoparticle dose required to  
336 provide effective radiosensitization, which is further confounded by the variety of particles studied  
337 in various research labs. Additionally, these surfaces can be used to explore the topological effects  
338 on cell growth and differentiation, and application of reduced laser doses can be used to potentially  
339 drive differentiation in key directions. Ultimately, these types of surfaces allow for control of some  
340 of the variables at play in nanomedicine. They present an avenue for greater understanding of the  
341 interactions at the interface between nanotechnology and biology.

## 342 **Conclusion**

343 Generating surfaces of known particle density allowed for more accurate determination of the  
344 effect of nanoregional heating in the current study. By coating the particles on the surface, the  
345 number of particles directly contacting each cell can be more tightly controlled and the number of  
346 particles per unit area of the membrane can be optimized for a given experimental goal. The  
347 fabrication method we have developed for our cell cultures securely attaches gold nanoparticles to  
348 glass. This method's utility was demonstrated with a variety of nanoparticle morphologies  
349 including Au nanocages, nanorods, and nanospheres. SEM validated a uniform distribution,  
350 particularly in relation to the size of a mammalian cell. Nanocages that were roughly 50 nm across  
351 were used as a model system to demonstrate the highly localized effects of nanoparticle heating  
352 by absorption of near infrared laser and the failure of bulk temperature measurements to accurately  
353 predict outcomes. The nanomaterial coated surfaces appear to be useful for a variety of in vitro,  
354 pre-clinical investigations and ultimately may predict in vivo performance of various  
355 nanomedicines.

## 356 **Declarations**

357 *Ethics Approval and Consent to Participate*

358 This work did not include or animal subject. Experiments were performed in compliance with  
359 institutional biosafety and biosecurity protocols.

360 *Consent for Publication*

361 No images of human subjects are included in this work.

362 *Availability of Data and Material*

363 Data sharing is not applicable to this article as no datasets were generated or analysed during the  
364 current study.

365 *Competing Interests*

366 The Authors declare no competing financial interest

367 *Funding*

368 Funding for this work was provided by National Science Foundation EPSCoR RIII Award  
369 1457888 and the Translational Research Institute grant TL1 TR003109 through the National  
370 Center for Advancing Translational Sciences of the National Institutes of Health (NIH).

371 *Authors' Contributions*

372 SVJ: Conceptualization, Methodology, Investigation, Writing Original Draft, Review Editing,

373 SJ: Methodology, Investigation, Writing Original Draft, Writing Review Editing

374 SS: Investigation

375 PM: Methodology, Investigation, Writing original draft, Writing review editing

376 RD: Conceptualization, Resources, Writing Review editing, Supervision

377 MB: Conceptualization, Methodology, Resources, Writing review editing, Supervision, Funding  
378 Acquisition

379 RG: Conceptualization, Methodology, Resources, Writing Original Draft, Review Editing,  
380 Supervision, Funding Acquisition

381 *Acknowledgements*

382 The authors thank J. Chen for providing facilities for AuNC synthesis, P. Corry, N. Koonce, and  
383 J. Bischof for helpful discussion.

## 384 **REFERENCES**

- 385 1. Sharma, S. K.; Shrivastava, N.; Rossi, F.; Tung, L. D.; Thanh, N. T. K., Nanoparticles-  
386 based magnetic and photo induced hyperthermia for cancer treatment. *Nano Today* **2019**, *29*,  
387 100795.
- 388 2. Wilets, K. A.; Duyne, R. P. V., Localized Surface Plasmon Resonance Spectroscopy and  
389 Sensing. *Annual Review of Physical Chemistry* **2007**, *58*, 267-97.
- 390 3. Schöttler, S.; Becker, G.; Winzen, S.; Steinbach, T.; Mohr, K.; Landfester, K.;  
391 Mailänder, V.; Wurm, F. R., Protein adsorption is required for stealth effect of poly(ethylene  
392 glycol)- and poly(phosphoester)-coated nanocarriers. *Nature Nanotechnology* **2016**, *11*, 372.
- 393 4. Zhou, J.; Ralston, J.; Sedev, R.; Beattie, D. A., Functionalized gold nanoparticles:  
394 Synthesis, structure and colloid stability. *Journal of Colloid and Interface Science* **2009**, *331* (2),  
395 251-262.
- 396 5. Srivatsan, A.; Jenkins, S. V.; Jeon, M.; Wu, Z.; Kim, C.; Chen, J.; Pandey, R. K., Gold  
397 nanocage-photosensitizer conjugates for dual-modal image-guided enhanced photodynamic  
398 therapy. *Theranostics* **2014**, *4* (2), 163-74.
- 399 6. Jenkins, S. V.; Qu, H.; Mudalige, T.; Ingle, T. M.; Wang, R.; Wang, F.; Howard, P.  
400 C.; Chen, J.; Zhang, Y., Rapid determination of plasmonic nanoparticle agglomeration status in  
401 blood. *Biomaterials* **2015**, *51* (0), 226-237.

- 402 7. Wang, H.; Chen, B.; He, M.; Li, X.; Chen, P.; Hu, B., Study on uptake of gold  
403 nanoparticles by single cells using droplet microfluidic chip-inductively coupled plasma mass  
404 spectrometry. *Talanta* **2019**, *200*, 398-407.
- 405 8. Rosman, C.; Pierrat, S.; Henkel, A.; Tarantola, M.; Schneider, D.; Sunnick, E.;  
406 Janshoff, A.; Sönnichsen, C., A New Approach to Assess Gold Nanoparticle Uptake by  
407 Mammalian Cells: Combining Optical Dark-Field and Transmission Electron Microscopy. *Small*  
408 **2012**, *8* (23), 3683-3690.
- 409 9. Jenkins, S. V.; Nima, Z. A.; Vang, K. B.; Kannarpady, G.; Nedosekin, D. A.; Zharov,  
410 V. P.; Griffin, R. J.; Biris, A. S.; Dings, R. P. M., Triple-negative breast cancer targeting and  
411 killing by EpCAM-directed, plasmonically active nanodrug systems. *npj Precision Oncology*  
412 **2017**, *1* (1), 27.
- 413 10. Yuan, H.; Fales, A. M.; Vo-Dinh, T., TAT Peptide-Functionalized Gold Nanostars:  
414 Enhanced Intracellular Delivery and Efficient NIR Photothermal Therapy Using Ultralow  
415 Irradiance. *Journal of the American Chemical Society* **2012**, *134* (28), 11358-11361.
- 416 11. Untener, E. A.; Comfort, K. K.; Maurer, E. I.; Grabinski, C. M.; Comfort, D. A.;  
417 Hussain, S. M., Tannic Acid Coated Gold Nanorods Demonstrate a Distinctive Form of  
418 Endosomal Uptake and Unique Distribution within Cells. *ACS Applied Materials & Interfaces*  
419 **2013**, *5* (17), 8366-8373.
- 420 12. Gu, Y.-J.; Cheng, J.; Lin, C.-C.; Lam, Y. W.; Cheng, S. H.; Wong, W.-T., Nuclear  
421 penetration of surface functionalized gold nanoparticles. *Toxicology and Applied Pharmacology*  
422 **2009**, *237* (2), 196-204.

- 423 13. Merzel, R. L.; Orr, B. G.; Banaszak Holl, M. M., Distributions: The Importance of the  
424 Chemist's Molecular View for Biological Materials. *Biomacromolecules* **2018**, *19* (5), 1469-  
425 1484.
- 426 14. Coradeghini, R.; Gioria, S.; García, C. P.; Nativo, P.; Franchini, F.; Gilliland, D.;  
427 Ponti, J.; Rossi, F., Size-dependent toxicity and cell interaction mechanisms of gold  
428 nanoparticles on mouse fibroblasts. *Toxicology Letters* **2013**, *217* (3), 205-216.
- 429 15. Haiss, W.; Thanh, N. T. K.; Aveyard, J.; Fernig, D. G., Determination of Size and  
430 Concentration of Gold Nanoparticles from UV-Vis Spectra. *Analytical Chemistry* **2007**, *79* (11),  
431 4215-4221.
- 432 16. Zlatanova, J.; van Holde, K., Single-Molecule Biology: What Is It and How Does It  
433 Work? *Molecular Cell* **2006**, *24* (3), 317-329.
- 434 17. Ali, M. R. K.; Wu, Y.; El-Sayed, M. A., Gold-Nanoparticle-Assisted Plasmonic  
435 Photothermal Therapy Advances Toward Clinical Application. *The Journal of Physical*  
436 *Chemistry C* **2019**, *123* (25), 15375-15393.
- 437 18. Dewey, W. C., Arrhenius relationships from the molecule and cell to the clinic.  
438 *International Journal of Hyperthermia* **1994**, *10* (4), 457-483.
- 439 19. Pearce, J., *Relationship between Arrhenius models of thermal damage and the CEM 43*  
440 *thermal dose*. SPIE: 2009; Vol. 7181.
- 441 20. Behrouzkia, Z.; Joveini, Z.; Keshavarzi, B.; Eyvazzadeh, N.; Aghdam, R. Z.,  
442 Hyperthermia: How Can It Be Used? *Oman Medical Journal* **2016**, *31* (2), 89-97.
- 443 21. Creixell, M.; Bohórquez, A. C.; Torres-Lugo, M.; Rinaldi, C., EGFR-Targeted Magnetic  
444 Nanoparticle Heaters Kill Cancer Cells without a Perceptible Temperature Rise. *ACS Nano* **2011**,  
445 *5* (9), 7124-7129.

- 446 22. Gerner, E. W., Thermal dose and time—temperature factors for biological responses to  
447 heat shock. *International Journal of Hyperthermia* **1987**, 3 (4), 319-327.
- 448 23. van Rhoon, G. C.; Samaras, T.; Yarmolenko, P. S.; Dewhirst, M. W.; Neufeld, E.;  
449 Kuster, N., CEM43°C thermal dose thresholds: a potential guide for magnetic resonance  
450 radiofrequency exposure levels? *European radiology* **2013**, 23 (8), 2215-2227.
- 451 24. Borrelli, M. J.; Thompson, L. L.; Cain, C. A.; Dewey, W. C., Time-temperature analysis  
452 of cell killing of BHK cells heated at temperatures in the range of 43.5°C to 57.0°C.  
453 *International Journal of Radiation Oncology\*Biology\*Physics* **1990**, 19 (2), 389-399.
- 454 25. Garanina, A. S.; Naumenko, V. A.; Nikitin, A. A.; Myrovali, E.; Petukhova, A. Y.;  
455 Klimyuk, S. V.; Nalench, Y. A.; Ilyasov, A. R.; Vodopyanov, S. S.; Erofeev, A. S.; Gorelkin,  
456 P. V.; Angelakeris, M.; Savchenko, A. G.; Wiedwald, U.; Majouga Dr, A. G.; Abakumov, M.  
457 A., Temperature-controlled magnetic nanoparticles hyperthermia inhibits primary tumor growth  
458 and metastases dissemination. *Nanomedicine: Nanotechnology, Biology and Medicine* **2020**,  
459 102171.
- 460 26. Li, Z.; Huang, P.; Zhang, X.; Lin, J.; Yang, S.; Liu, B.; Gao, F.; Xi, P.; Ren, Q.; Cui,  
461 D., RGD-Conjugated Dendrimer-Modified Gold Nanorods for in Vivo Tumor Targeting and  
462 Photothermal Therapy. *Molecular Pharmaceutics* **2010**, 7 (1), 94-104.
- 463 27. Zhang, S.; Li, Y.; He, X.; Dong, S.; Huang, Y.; Li, X.; Li, Y.; Jin, C.; Zhang, Y.;  
464 Wang, Y., Photothermolysis mediated by gold nanorods modified with EGFR monoclonal  
465 antibody induces Hep-2 cells apoptosis in vitro and in vivo. *International journal of*  
466 *nanomedicine* **2014**, 9, 1931-1946.
- 467 28. Jenkins, S. V.; Nedosekin, D. A.; Shaulis, B. J.; Wang, T.; Jamshidi-Parsian, A.;  
468 Pollock, E. D.; Chen, J.; Dings, R. P. M.; Griffin, R. J., Enhanced Photothermal Treatment

469 Efficacy and Normal Tissue Protection via Vascular Targeted Gold Nanocages.  
470 *Nanotheranostics* **2019**, 3 (2), 145-155.

471 29. Jenkins, S. V.; Nedosekin, D. A.; Miller, E. K.; Zharov, V. P.; Dings, R. P. M.; Chen,  
472 J.; Griffin, R. J., Galectin-1-based tumour-targeting for gold nanostructure-mediated  
473 photothermal therapy. *International Journal of Hyperthermia* **2018**, 34 (1), 19-29.

474 30. Meeker, D. G.; Jenkins, S. V.; Miller, E. K.; Beenken, K. E.; Loughran, A. J.;  
475 Powless, A.; Muldoon, T. J.; Galanzha, E. I.; Zharov, V. P.; Smeltzer, M. S.; Chen, J.,  
476 Synergistic Photothermal and Antibiotic Killing of Biofilm-Associated *Staphylococcus aureus*  
477 Using Targeted Antibiotic-Loaded Gold Nanoconstructs. *ACS Infectious Diseases* **2016**, 2 (4),  
478 241-250.

479 31. Zhang, Y.; Zhan, X.; Xiong, J.; Peng, S.; Huang, W.; Joshi, R.; Cai, Y.; Liu, Y.; Li,  
480 R.; Yuan, K.; Zhou, N.; Min, W., Temperature-dependent cell death patterns induced by  
481 functionalized gold nanoparticle photothermal therapy in melanoma cells. *Scientific Reports*  
482 **2018**, 8 (1), 8720.

483 32. Carlson, M. T.; Khan, A.; Richardson, H. H., Local Temperature Determination of  
484 Optically Excited Nanoparticles and Nanodots. *Nano Letters* **2011**, 11 (3), 1061-1069.

485 33. Baffou, G.; Berto, P.; Bermúdez Ureña, E.; Quidant, R.; Monneret, S.; Polleux, J.;  
486 Rigneault, H., Photoinduced Heating of Nanoparticle Arrays. *ACS Nano* **2013**, 7 (8), 6478-6488.

487 34. Skrabalak, S. E.; Au, L.; Li, X.; Xia, Y., Facile synthesis of Ag nanocubes and Au  
488 nanocages. *Nat Protoc* **2007**, 2 (9), 2182-90.

489 35. Govorov, A. O.; Zhang, W.; Skeini, T.; Richardson, H.; Lee, J.; Kotov, N. A., Gold  
490 nanoparticle ensembles as heaters and actuators: melting and collective plasmon resonances.  
491 *Nanoscale Research Letters* **2006**, 1 (1), 84.

- 492 36. van Dommelen, R.; Fanzio, P.; Sasso, L., Surface self-assembly of colloidal crystals for  
493 micro- and nano-patterning. *Advances in Colloid and Interface Science* **2018**, *251*, 97-114.
- 494 37. Xue, Y.; Li, X.; Li, H.; Zhang, W., Quantifying thiol–gold interactions towards the  
495 efficient strength control. *Nature Communications* **2014**, *5*, 4348.
- 496 38. Ansar, S. M.; Ameer, F. S.; Hu, W.; Zou, S.; Pittman, C. U.; Zhang, D., Removal of  
497 Molecular Adsorbates on Gold Nanoparticles Using Sodium Borohydride in Water. *Nano Letters*  
498 **2013**, *13* (3), 1226-1229.

## 499 **Figure Captions**

500 **Table 1** – Synthetic Parameters and outcomes.

501

502 **Scheme 1** – Fabrication of strongly bound AuNP-coated glass coverslips.

503

504 **Figure 1** – Optical characterization of AuNC coated surfaces. (A) Photograph of AuNC-coated  
505 surfaces with varying coverage densities. (B-E) Optical microscopy (10x magnification) of the  
506 coated surfaces). (F) Extinction spectra of coated surfaces with varying densities.

507

508 **Figure 2** – Scanning electron microscopy and quantification of AuNC coated surfaces. Reaction  
509 AuNC quantities and resultant coverage densities (mean  $\pm$  s.d.) of (A) 0, 0; (B) 6.4 fmol,  $20 \pm 2$   
510 AuNC/ $\mu\text{m}^2$ ; (C) 12.8 fmol,  $32 \pm 2$  AuNC/ $\mu\text{m}^2$ ; (D) 25.6 fmol,  $54 \pm 2$  AuNC/ $\mu\text{m}^2$ .

511

512 **Figure 3** Kinetics of AuNC deposition. (A) Extinction spectra, (B) coverage density (mean  $\pm$  s.d.),  
513 and (C) corresponding SEM for AuNC coated surfaces generated using 12.8 fmol AuNC.

514

515 **Figure 4** – Scanning Electron microscopy of other AuNP morphologies. (A) Au rods (11x47 nm),  
516 (B) 50 nm Au spheres, (C) 5 nm Au spheres with 100 nm scale bars.

517

518 **Figure 5** – Laser heating of AuNC coated surfaces. (A) Surface temperature of the 32 AuNC/ $\mu\text{m}^2$   
519 coated surface with varying laser output. (B) Surface temperature during 1.5 W (0.75 W/cm<sup>2</sup>)  
520 irradiation with AuNC coated surface of varying coverage density. SEM images of AuNC coated  
521 surfaces after thermal treatment (C) before and (D) after rinsing with DMSO. Data presented are  
522 mean  $\pm$  s.d.

523

524 **Figure 6** – Theoretical calculations of temperature versus distance from the AuNC-coated surface.  
525 (A) Temperature change versus distance as calculated from Eq. (3). The inset shows the same  
526 curve but with a smaller range of distance. (B) Temperature versus distance for increasing time.  
527 The temperature values were calculated by adding the shown  $T_\infty$  values for each time to the  
528 temperature change curve shown in (A). The inset shows the same curves but with a smaller range  
529 of distance. (C) Theoretical thermal dose (cumulative equivalent minutes at 43 °C; CEM43) based  
530 on average temperature experienced across 5  $\mu\text{m}$  outward from the particle surface.

531

532 **Figure 7** – Cell viability as a function of heating. (A) Viability of EL4 (crossed, red) and 4T1  
533 (slashed, blue) cells following laser irradiation or bulk heating normalized to untreated cells on a  
534 standard tissue culture plate. (B) Viability response of 4T1 cells to bulk heating for 10 min. Data  
535 presented are mean  $\pm$  s.d.

536

# Figures

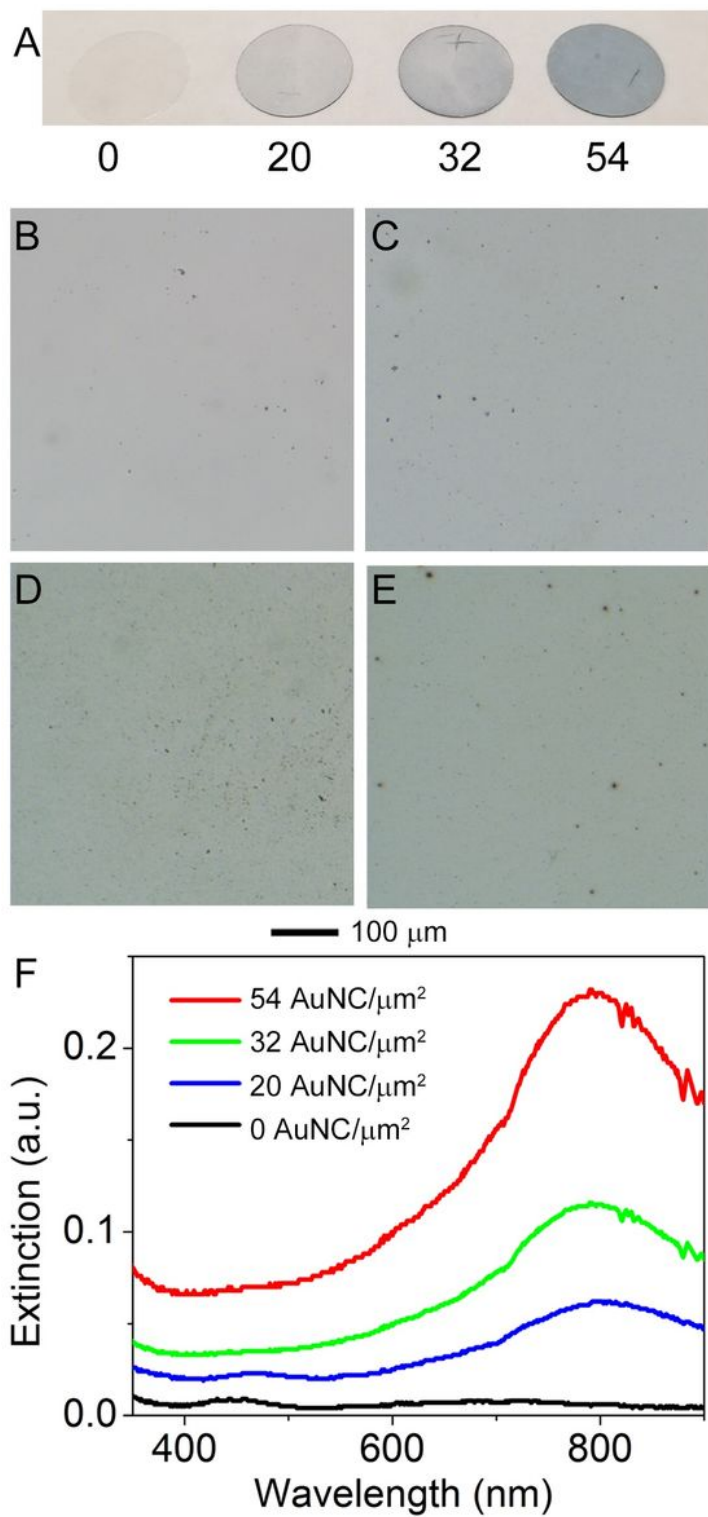


**Figure 1**

Optical characterization of AuNC coated surfaces. (A) Photograph of AuNC-coated surfaces with varying coverage densities. (B-E) Optical microscopy (10x magnification) of the coated surfaces. (F) Extinction spectra of coated surfaces with varying densities.

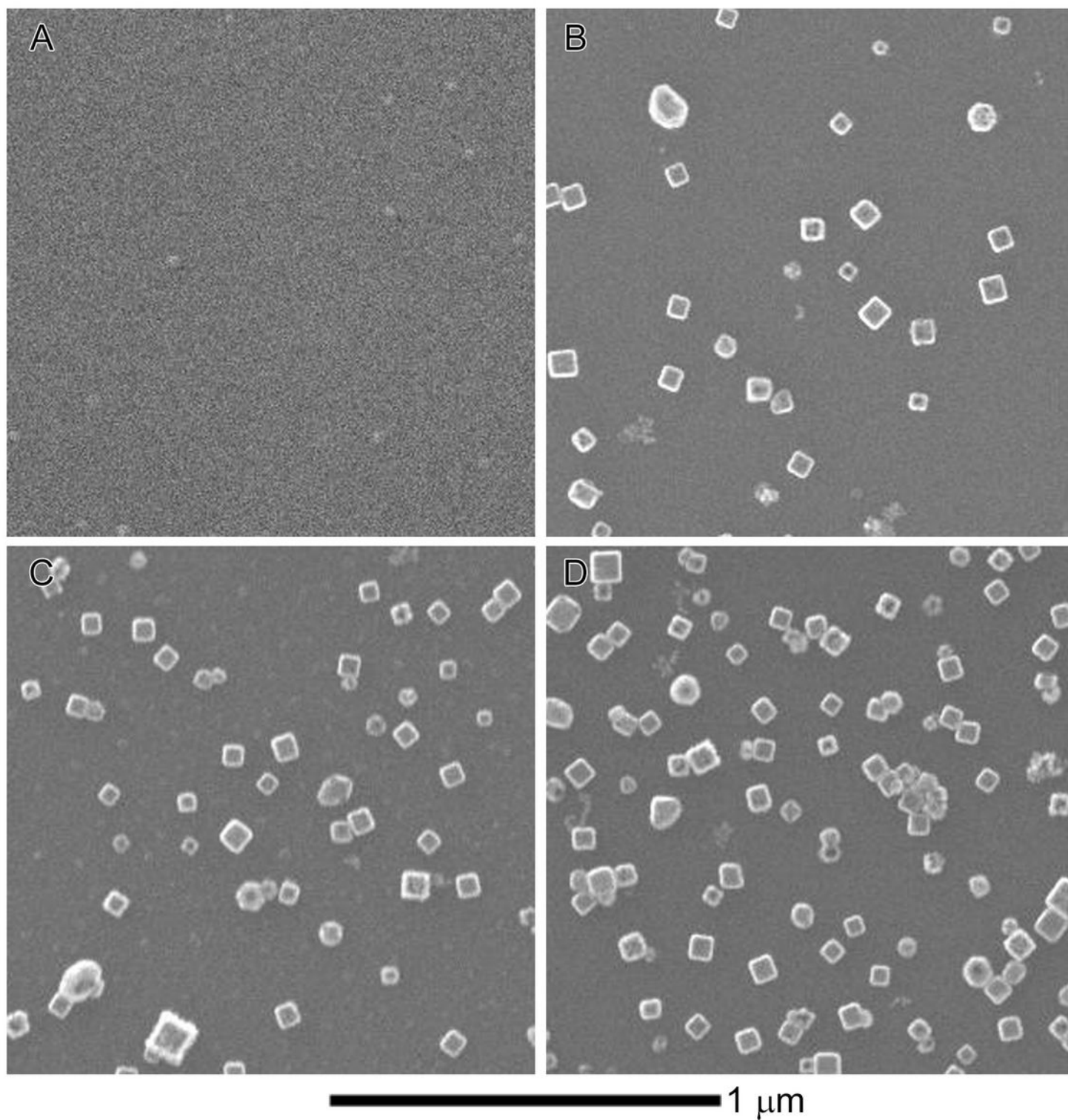


**Figure 2**

Scanning electron microscopy and quantification of AuNC coated surfaces. Reaction AuNC quantities and resultant coverage densities (mean  $\pm$  s.d.) of (A) 0, 0; (B) 6.4 fmol,  $20 \pm 2$  AuNC/ $\mu\text{m}^2$ ; (C) 12.8 fmol,  $32 \pm 2$  AuNC/ $\mu\text{m}^2$ ; (D) 25.6 fmol,  $54 \pm 2$  AuNC/ $\mu\text{m}^2$ .

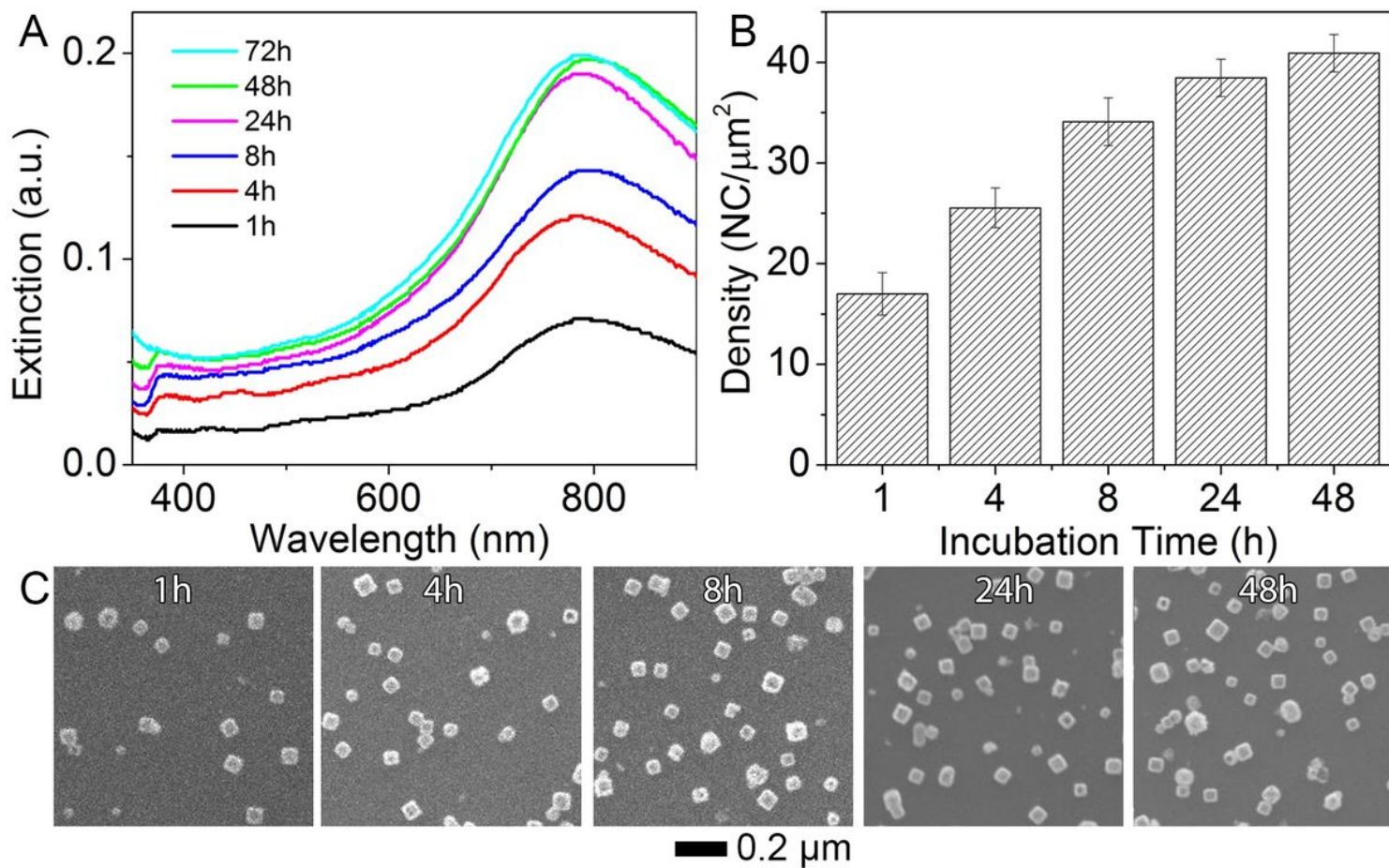


**Figure 3**

Kinetics of AuNC deposition. (A) Extinction spectra, (B) coverage density (mean  $\pm$  s.d.), and (C) corresponding SEM for AuNC coated surfaces generated using 12.8 fmol AuNC.

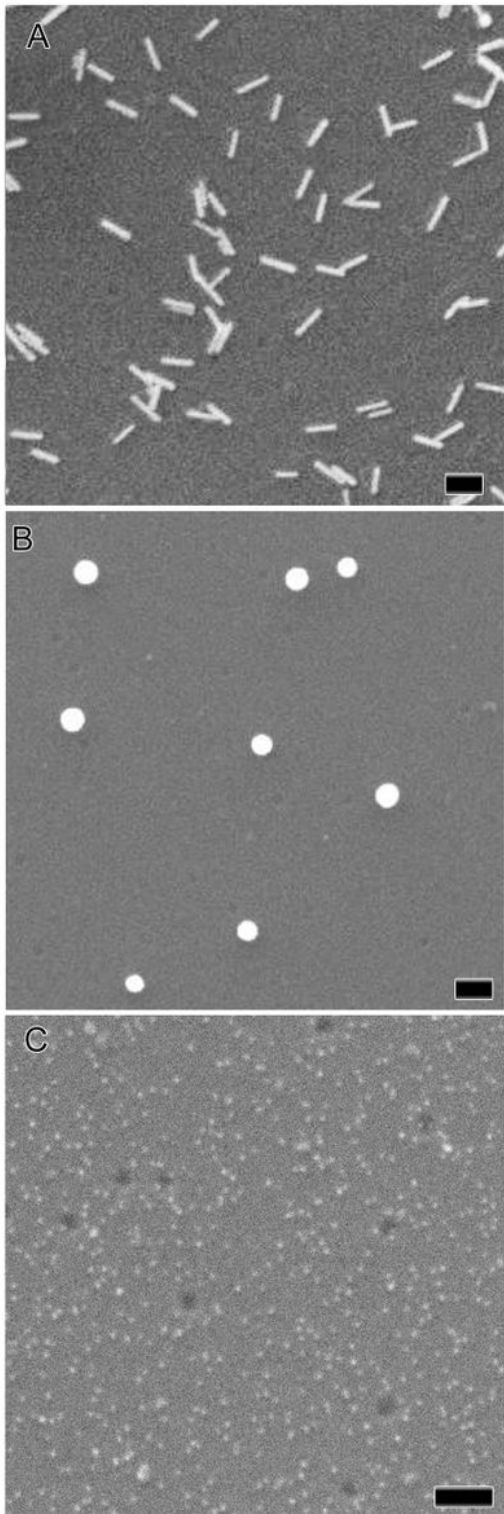


**Figure 4**

Scanning Electron microscopy of other AuNP morphologies. (A) Au rods (11x47 nm), (B) 50 nm Au spheres, (C) 5 nm Au spheres with 100 nm scale bars.

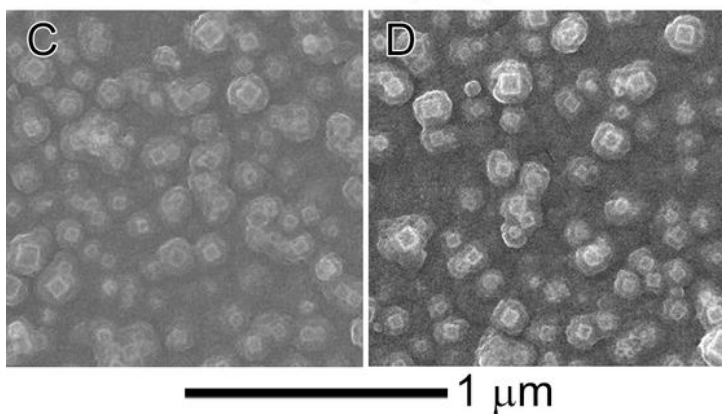
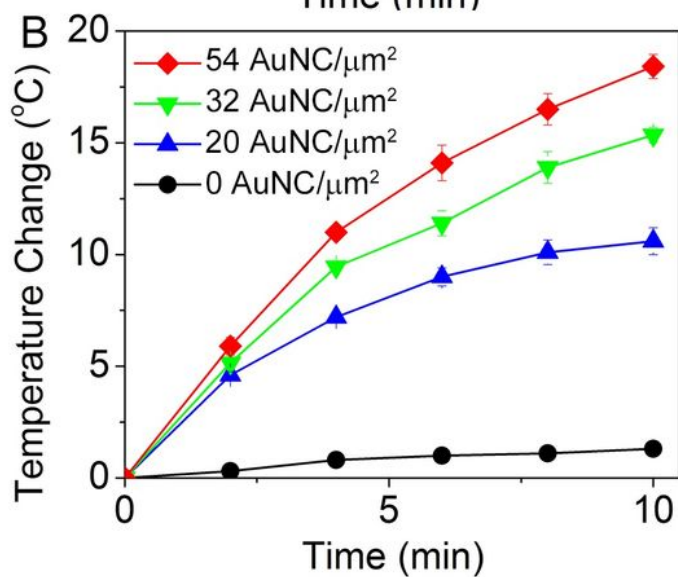
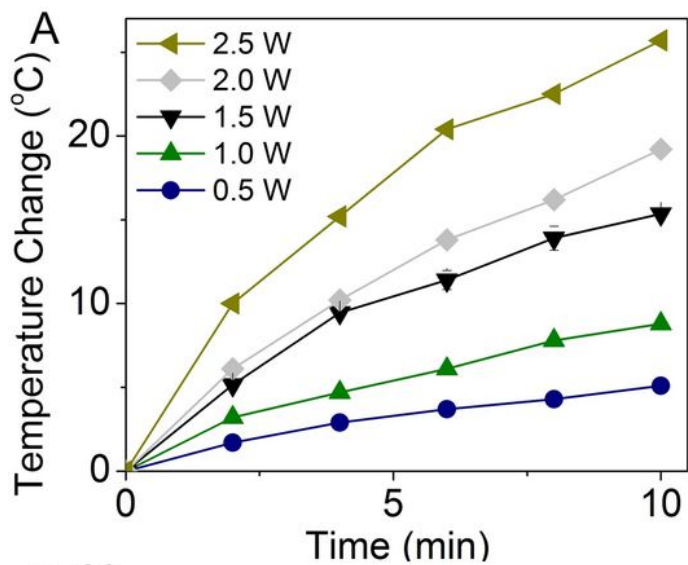


**Figure 5**

Laser heating of AuNC coated surfaces. (A) Surface temperature of the 32 AuNC/ $\mu\text{m}^2$  coated surface with varying laser output. (B) Surface temperature during 1.5 W ( $0.75 \text{ W}/\text{cm}^2$ ) irradiation with AuNC coated surface of varying coverage density. SEM images of AuNC coated surfaces after thermal treatment (C) before and (D) after rinsing with DMSO. Data presented are mean  $\pm$  s.d.

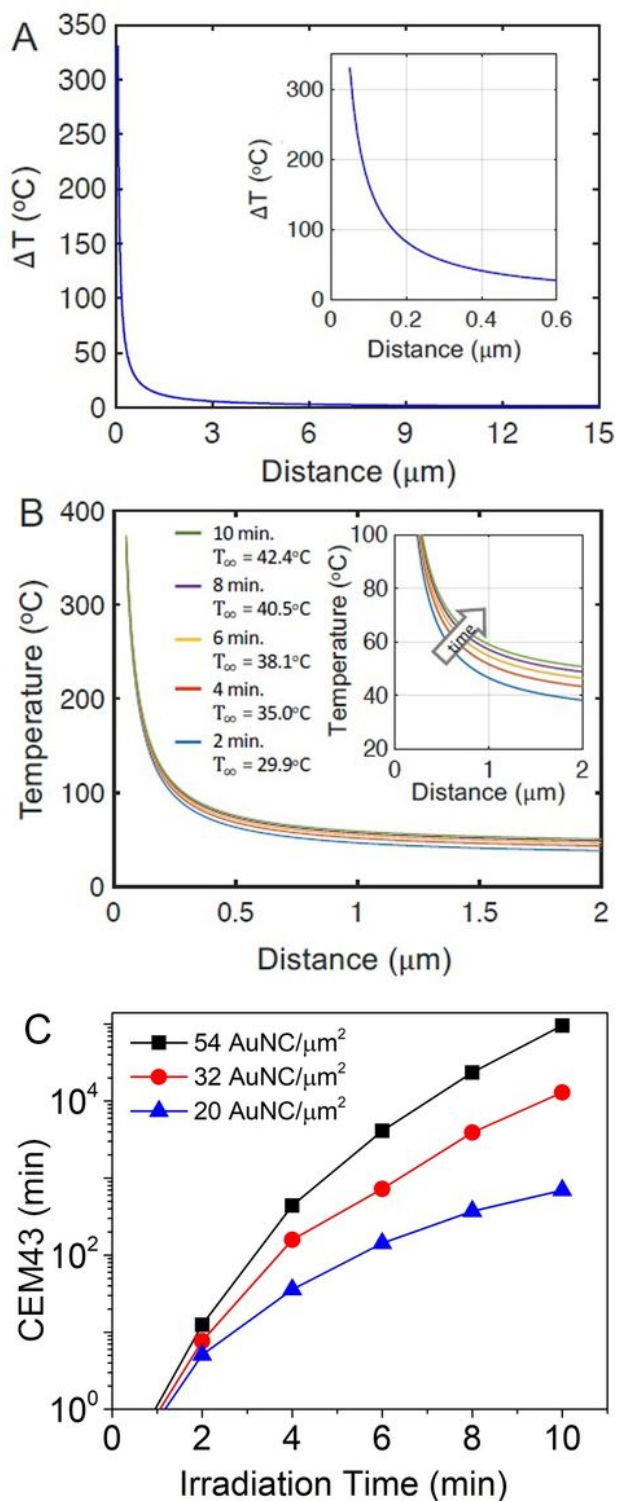


**Figure 6**

Theoretical calculations of temperature versus distance from the AuNC-coated surface. (A) Temperature change versus distance as calculated from Eq. (3). The inset shows the same curve but with a smaller range of distance. (B) Temperature versus distance for increasing time. The temperature values were calculated by adding the shown  $T_{\infty}$  values for each time to the temperature change curve shown in (A). The inset shows the same curves but with a smaller range of distance. (C) Theoretical thermal dose

(cumulative equivalent minutes at 43 °C; CEM43) based on average temperature experienced across 5  $\mu\text{m}$  outward from the particle surface.

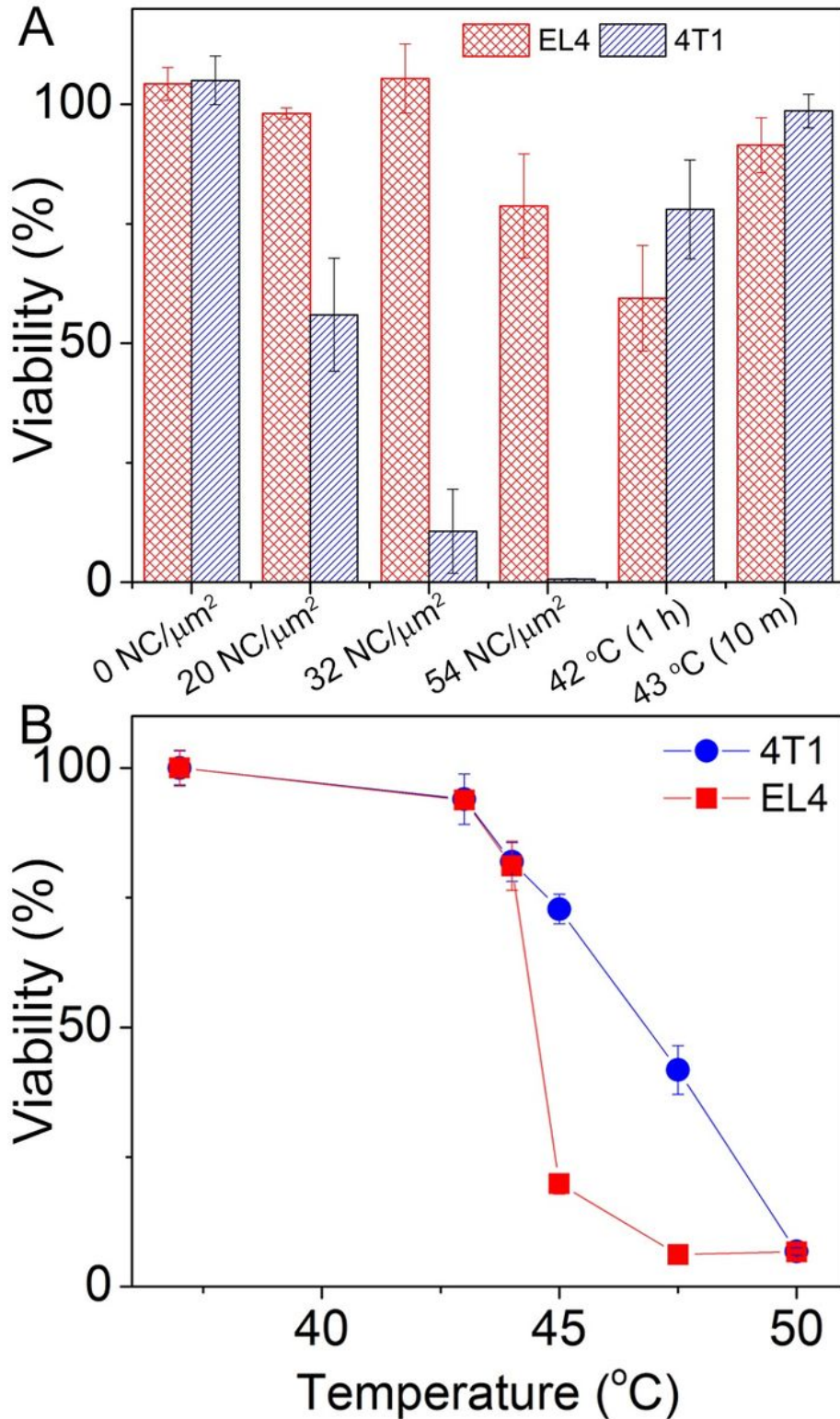
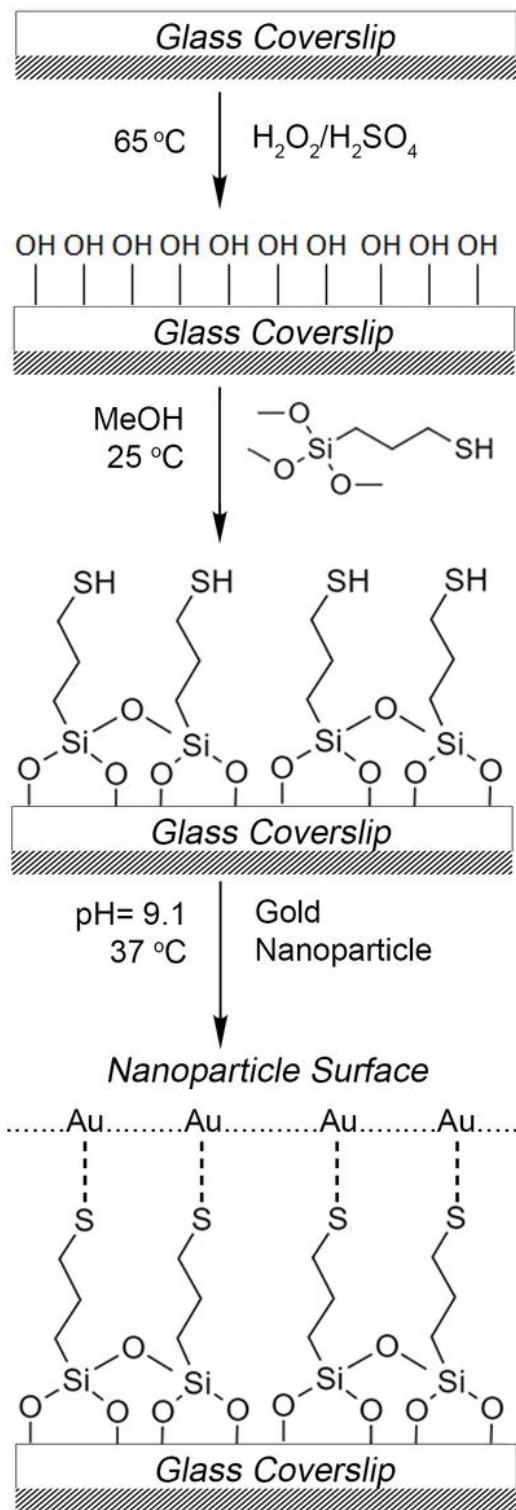


Figure 7

Cell viability as a function of heating. (A) Viability of EL4 (crossed, red) and 4T1 (slashed, blue) cells following laser irradiation or bulk heating normalized to untreated cells on a standard tissue culture plate. (B) Viability response of 4T1 cells to bulk heating for 10 min. Data presented are mean  $\pm$  s.d.



**Figure 8**

Scheme 1 – Fabrication of strongly bound AuNP-coated glass coverslips.

## Supplementary Files

This is a list of supplementary files associated with this preprint. Click to download.

- [Table1.pdf](#)